Bismuth ferrite-based lead free ceramics and multilayers with high recoverable energy density

Dawei Wang[a]*, Zhongming Fan[b], Di Zhou[a,c], Amir Khesro[a,d], Shunsuke Murakami[a], Antonio Feteira[e], Quanliang Zhao[f], Xiaoli Tan[b], Ian M Reaney[a]*

[a]*Department of Materials Science and Engineering, University of Sheffield, Sheffield S1 3JD, UK*

[b]*Department of Materials Science and Engineering, Iowa State University, Ames, Iowa, 50011 USA*

[c]*Electronic Materials Research Laboratory, Key Laboratory of the Ministry of Education & International Center for Dielectric Research, Xi'an Jiaotong University, Xi'an 710049, Shaanxi, China*

[d]*Department of Physics Abdul Wali Khan University, Garden Campus 23200, Mardan. Pakistan*

[e]*Christian Doppler Laboratory for Advanced Ferroic Oxides, Sheffield Hallam University, Sheffield S1 1WB, UK*

[f]*School of Mechanical and Materials Engineering, North China University of Technology, Beijing 100144, China*

* Corresponding author. E-mail address: dawei.wang@sheffield.ac.uk, i.m.reaney@sheffield.ac.uk

Abstract:

Lead-free ceramics with high recoverable energy density (W_{rec}) and energy storage efficiency (η) are attractive for advanced pulsed power capacitors to enable greater miniaturization and integration. In this work, dense bismuth ferrite (BF)-based, lead-free $0.75(Bi_{1-x}Nd_x)FeO_3$-$0.25BaTiO_3$ (BNxF-BT) ceramics and multilayers were fabricated. A transition from a mixed pseudocubic and *R3c* to a purely pseudocubic structure was observed as x increased with optimum properties obtained for mixed compositions. Highest energy densities, $W \sim 4.1$ J/cm^3 and $W_{rec} \sim 1.82$ J/cm^3 were achieved for BN15F-BT, due to the enhanced breakdown field strength (BDS ~ 180 kV/cm) and large maximum polarization ($P_{max} \sim 40$ μC/cm^2). Multilayers of this composition possessed both high W_{rec} of 6.74 J/cm^3 and η of 77% and were stable up to 125 °C. Nd doped BF-based ceramics with enhanced BDS and large W_{rec} are therefore considered promising candidates for lead-free energy storage applications.

Keywords: Energy storage, Bismuth ferrite, Lead-free ceramics, Dielectrics

1. Introduction

Materials with higher energy and power density are urgently needed to meet the growing demand in power supply components of portable electronics, power electronics, electrical vehicles and other energy storage devices.[1-3] Compared to other energy storage devices (such as fuel cells, batteries, and electrochemical capacitors), dielectric capacitors have received particular attention for advanced pulsed power because of their high power density and quick charge-discharge rate.[4-7] In general, three kinds of dielectric materials are used in capacitors: linear dielectrics; anti-ferroelectrics (AFE) and ferroelectrics (FE). For linear dielectrics energy density (W) is defined as:

$$W = ½\ DE = ½\ \varepsilon_r\varepsilon_0 E^2, \quad (1)$$

where D is the electrical displacement, ε_r is the dielectric constant, ε_0 is the vacuum permittivity and E is the applied-electrical field. Both high ε_r and E are required to achieve high W for linear dielectrics. For AFE and FE, W, recoverable energy density (W_{rec}) and energy storage efficiency (η) are calculated by:

$$W = \int_0^{P_{max}} EdP, \quad (2)$$

$$W_{rec} = \int_{P_r}^{P_{max}} EdP, \quad (3)$$

$$\eta = W_{rec}/W \quad (4)$$

where P, P_{max} and P_r is the polarization, maximum polarization and remnant polarization, respectively. To achieve high W_{rec} and η, large P_{max}, small P_r and high electric breakdown strength (BDS) are simultaneously required.

Currently, polymers and ceramics dominate the dielectric materials used in solid-state capacitors. However, polymer-based dielectrics with high W resulting from high BDS, are usually limited to <100°C, due to their low melting temperatures.[8,9] Dielectric ceramics therefore, offer a viable option to develop high voltage-capable, high energy density, mechanically and thermally stable capacitors which operate at elevated temperatures. Lead-based dielectric ceramics have already proven to have potential in the application of energy-storage capacitors, with high W_{rec} (6.4 J/cm^{-3}) reported in La-doped Pb(Zr,Ti)O_3-based AFE ceramics fabricated by spark plasma sintering (SPS).[10-15] However, environmental issues, health concerns and regulations against hazardous substances in electric and

electronic equipment have stimulated research in lead-free materials for energy-storage.[16-18]

Lead-free energy storage ceramics such as $BaTiO_3$ (BT), $(Bi_{0.5}Na_{0.5})TiO_3$ (BNT) and $(K_{0.5}Na_{0.5})NbO_3$ (KNN)-based ceramics have been extensively investigated.[19-31] Initially, oxide additives such as Al_2O_3, SiO_2, MgO were reported to enhance the BDS and W_{rec} in BT-based ceramics[20-22] but more recently BT-$Bi(M_{2/3}Nb_{1/3})O_3$ and BT-$Bi(M_{1/2}Ti_{1/2})O_3$ (M = Mg and Zn) ceramics were studied, in which W_{rec} was reported up to 1~2 J/cm^3.[23-27] In addition, $Bi_{0.5}Na_{0.5}TiO_3$-$BaTiO_3$-$KNbO_3$ (BNT-BT-KN) and $Bi_{0.5}Na_{0.5}TiO_3$-$BaTiO_3$-$NaTaO_3$ (BNT-BT-NT) ceramics were also reported to achieve high W_{rec} of 1.72 and 1.2 J/cm^3, respectively.[28,29] Recently, Du et al. obtained very high BDS (300~400kV/cm) in KNN-based ceramics by controlling grain growth; hence W_{rec} was enhanced to ~ 4 J/cm^3.[30,31] $BiFeO_3$-$BaTiO_3$ (BF-BT) has been shown to have high Curie temperature (T_C) and a large polarization at its structural phase boundary (P_{max} > 40 μC/cm^2).[32-35] However, due to its high dielectric loss and P_r, the energy storage properties of BF-BT have rarely been studied. Recently, Wang and Zheng et al. introduced Nb, $Ba(Mg_{1/3}Nb_{2/3})O_3$ and $La(Mg_{1/2}Ti_{1/2})O_3$ into BF-BT and reported W_{rec} of 0.71, 1.56 and 1.66 J/cm^3, respectively, suggesting that BF-BT solid solutions are promising candidates for energy storage materials and devices.[36-38] More recently, Xu et al. theoretically predicted that Nd-doped BF based ceramics could potentially allow high energy densities (100-150 J/cm^3) and efficiencies (80-88%).[39] However, to our knowledge, there is no reported experimental work on the effect of Nd doping on the energy storage properties of BF-based systems. The composition dependence of structural, dielectric, ferroelectric, high-field strain and energy storage of Nd doped BF-BT ceramics and multilayers are therefore investigated. Multilayers fabricated with Pt internal electrodes yielded W_{rec} of 6.74 J/cm^3 and η of 77%, with the variation of W_{rec} ~15% from room temperature (RT) to 125 °C.

2. Experimental procedure

BF-BT ceramics with compositions of $0.75(Bi_{1-x}Nd_x)FeO_3$ - $0.25BaTiO_3$ + 0.1wt% MnO_2 (x = 0, 2.5%, 5%, 7.5%, 10%, 15%, 20%, 30% and 40%, abbreviated as BF-BT, BN2.5F-BT, BN5F-BT, BN7.5F-BT, BN10F-BT, BN15F-BT, BN20F-BT, BN30F-BT and BN40F-BT, respectively) were prepared using a conventional solid state reaction route. Multilayers were tapecasted with details of ceramic and multilayer fabrication reported elsewhere.[32,40] Densities of sintered samples were measured using the

Archimedes method. The structure and phase assemblage of the sintered samples were studied using a Bruker D2 Phaser X-ray powder diffraction (XRD). FEI Inspect F scanning electron microscope (SEM) and Tecnai G2-F20 transmission electron microscopy (TEM) were employed to reveal the grain and domain structure, respectively. For TEM, sintered pellets of BF-BT, BN5F-BT and BN10F-BT were mechanically ground and polished to 120 µm. Disks of 3 mm in diameter were ultrasonically cut and the center portion was thinned to 10 µm by mechanical dimpling. Disks were annealed at 550 °C, 400 °C and 300 °C for 0.5 hour to remove residual stresses followed by Ar-ion milling to the point of electron transparency. For electrical tests, sintered samples were electroded using fired-on silver paste, followed by poling in silicone oil at 100~120 °C with an applied electric field of ~ 60 kV/cm. The piezoelectric coefficient (d_{33}) was measured using a Piezotest PM300 d_{33} meter. Polarization hysteresis, leakage current density and strain-electric field behaviour were determined using an aixACCT TF 2000 ferroelectric tester at a frequency of 1 Hz from RT to 150 °C. The displacement data was synchronously captured by a laser interferometer. The temperature dependence of dielectric properties from RT to 600 °C was carried out using an Agilent 4184A multi-frequency precision LCR meter. The discharge properties were measured using a specially designed, high-speed capacitor discharge circuit similar to that reported in the literature.[19] The discharge current waveforms were obtained by an Tektronix DPO 4104 oscilloscope connected with a Pearson 6585 coil. The discharge energy was measured using a load resistor (RL) in series with the ceramic samples.

3. Results and discussion

The RT XRD patterns of BNxF-BT in the 2θ range of 20°~70° are shown in Fig. 1. All peaks were attributed to either a single or mixed perovskite phases. Diffraction peaks shifted to a higher diffraction angle with increasing Nd concentration, consistent with the smaller relative ionic radius of Nd^{3+} with respect to Bi^{3+} ions in the matrix.[41,42] Splitting of (021)/(110) diffraction peak at ~$2\theta = 32°$ is commonly used to determine the likely symmetry of compositions. From the expanded XRD patterns, the coexistence of two perovskite phases in the BF-BT, BN2.5F-BT and BN5F-BT is apparent at RT, as indicated by broad multiple peaks.[32,34] With increase in Nd concentration, a single pseudocubic (*PC*) phase gradually dominates.[32-34]

To further confirm structural evolution, Rietveld refinement of all studied compositions was performed using the GSAS+EXPGUI package,[43,44] in which a two-phase refinement ($R3c + Pm\bar{3}m$) was used. Good agreement between the observed and calculated patterns was obtained for all the compositions as shown in Table I and Fig. 2, in which the refinements of BF-BT and BN10F-BT were selected for comparison (Fig. 2a,b). As Nd concentration increased, the fraction of *R3c* phase in BNF-BT decreased from 65.2% for BF-BT to 27.9% for BN5F-BT and to 0 for higher Nd concentration (Table I), indicating the coexistence of *R* and *PC* phases with $x \leq 5\%$ and a single *PC* phase with $x > 5\%$. The unit cell volume of both *R* and *PC* phases decreased with increasing Nd concentration (Fig. 2c), consistent with a shift of XRD diffraction peaks to increasing 2θ (Fig. 1). There is an abrupt change in the lattice parameters of *R3c* phase for BN5F-BT (Fig. 2d). Whilst this does not indicate classic morphotropic phase boundary behaviour which is between two polar phases of different symmetry,[45] it implies a sharp rather than gradual loss of long range polar order as Nd concentration increases.

TEM images and selected area electron diffraction patterns (SADP) of BF-BT, BN5F-BT and BN10F-BT obtained with the electron parallel with a <110> axis are shown in Fig. 3 and Fig. 4. In BF-BT, the domain structure is complex with coarse herringbones-type domains separated by 71° domain walls on {110} planes, fine herringbones-type domains separated by 109° domain walls on {001} planes and complex submicron-sized domains.[46] An example of the fine herringbone macrodomain structure is given in Fig 3. In BN5F-BT, 80% of grains contain only nano-sized domains with the rest consisting of nano-sized and complex microdomains (Fig. 3), confirming its dominant pseudocubic nature. In contrast, all grains observed in BN10F-BT appeared domain-free (Fig 3). In BF-BT, ½{*ooo*} superlattice diffraction spots (Fig. 4) are observed which arise from rotations of the oxygen octahedra in antiphase, consistent with *R3c* symmetry with an $a^-a^-a^-$ tilt system[47] and with Rietveld refinements (Fig. 1 and 2 and Table I). Although the ½{*ooo*} superlattice reflections in BN5F-BT are weaker than those in BF-BT (Fig 4), they are still discrete (Fig 4), which indicates shorter correlation length and/or lesser magnitude of oxygen octahedral rotation in nano-sized regions in BN5F-BT with respect to the micron/submicron-sized domains in BF-BT. Despite the absence of an apparent domain structure, ½{*ooo*} type superlattice reflections are still observed in SADPs (Fig. 4), albeit weak and diffuse,

typical of short range order octahedral rotations. The ionic radius of Nd (1.27 Å) is smaller than that of Bi (1.35 Å)[48] and consequently the driving force for octahedral tilting (magnitude of octahedral rotation) according to tolerance factor arguments should increase and not decrease.[49] The decrease in intensity of the ½{*ooo*} superstructure reflection may therefore only be explained by frustration between the competing local structures. In $BiFeO_3$, the polar distortion is strongly coupled to the commensurate rotation of the octahedral cage around the [111] axis.[50,51] As the scale length of polar coupling decreases (as Nd concentration increases), so does the scale length of the octahedral rotations. Presumably, if the Nd concentration increases significantly further, long range octahedral tilting will re-emerge but most likely with a different tilt configuration, similar or related to that of the orthoferrites ($a^-a^-c^+$).[52]

The SEM images of BNxF-BT are shown in Fig. 5. All ceramics appear dense and pore-free, presenting a grain size distribution, in which small grains are interspaced with large grains. Based on the SEM images, the grain size distributions of BNxF-BT are given in the insets of Fig. 5, and the average grain size and relative density (ρ_r) of BNxF-BT as a function of Nd concentration is shown in Fig. 6. As Nd concentration increases, the grain size of BNxF-BT increases from 6.3 μm for BF-BT to 7.4 μm for BN2.5F-BT and then decreases to 1.9 μm for BN40F-BT, suggesting that high concentrations of Nd inhibit grain growth, possibly due the more refractory nature of Nd_2O_3.[34] At the same time, ρ_r improves from 95% for BF-BT to 97.6% for BN20F-BT but then remains constant with increasing Nd concentration. Small grain size and high density in bulk ceramics are believed to lead to high BDS which in turn enhances energy density.

The temperature dependence of dielectric permittivity (ε_r) and loss (*tanδ*) for BNxF-BT at 100 kHz is given in Fig. 7, with the corresponding T_C / maximum transition temperature (T_m) as a function of Nd concentration given in the inset of Fig. 7(b). With increasing Nd concentration, T_C/T_m decreases presumably due to the disruption of polar coupling by the substitution of the less polarisable Nd for Bi.[32,33] The decrease in polar coupling is also manifested in the appearance of broad frequency-dependent dielectric peaks, in agreement with the nano-sized domains in TEM images (Fig. 3). Despite these changes, the values of *tanδ* remain < 0.15 at < 300 °C, but then increase sharply (Fig. 7b), indicating an increase in dc conductivity at high temperature.

The high electric field bipolar polarization hysteresis (P-E) and unipolar strain (S-E) loops of BNxF-BT samples are shown in Fig. 8(a,b) (the strain of BNxF-BT with x > 15% was too low to be detected), from which P_r, coercive field (E_C) and average electric field induced maximum strain (S_{max}) as a function of Nd concentration are obtained. The effective high field piezoelectric strain coefficient (d_{33}^*) and hysteresis (SH) are calculated by

$$d_{33}^* = S_{max}/E_{max}, \quad (5)$$

$$SH = H_{Emax/2}/S_{max}, \quad (6)$$

respectively, where E_{max} is the maximum electric field value, $H_{Emax/2}$ is the width of the loop at half applied field.[53] Samples of BF-BT and BN2.5F-BT give saturated hysteresis loops (Fig. 8a) at 70 kV/cm, indicating high resistivity. As Nd concentration increased, the P-E loops became slimmer and unsaturated (Fig. 8a), with P_r, E_C and d_{33} continuously decreasing (Fig. 8c), indicative of relaxor-like behaviour, consistent with the broad permittivity maximum (Fig. 7a) and domain evolution (Fig. 3). The highest value of $P_r \sim 35$ μC/cm^2, $E_C \sim 53.9$ kV/cm, $d_{33} \sim 140$ pC/N and lowest value of HS ~ 18.4% is achieved for the 2.5%Nd doped BF-BT (Fig. 8c,d), due to the presence of mixed R3c and PC phases (Fig. 1 and 2).[32-34] At the same time, the highest value of $S_{max} \sim 0.14\%$, $d_{33}^* \sim 200$ pm/V and HS ~ 50% was obtained for BN5F-BT, Fig. 8(c, d), mainly attributed to the crossover from normal to relaxor ferroelectric behaviour (Fig. 3 and 7).[32]

Due to their slim P-E loops with low hysteresis loss (Fig. 7a), BNxF-BT with x > 10% were selected and polished to ~ 0.3 mm for further studies on their potential for energy storage. Unipolar P-E loops under different electric fields for BNxF-BT (x > 10%) are shown in Fig. 9 with the corresponding values of P_{max}, P_r and ΔP (P_{max} - P_r) as a function of electric field given in Fig. 10. As electric field increases, P_{max} and ΔP increase linearly with a slight increase of P_r for all studied compositions (Fig. 10). However, P_{max}, P_r and ΔP decrease at 170 kV/cm with increasing Nd concentration (in the inset of Fig. 10d), further confirming that Nd doping reduces polarization in BF-BT ceramics (Fig. 8a). The highest values of P_{max} and ΔP are 39.8, 23.5, 11.6, 7.8 μC/cm^2 and 30.7, 20.4, 10.7, 7.6 μC/cm^2 for BN15F-BT, BN20F-BT, BN30F-BT and BN40F-BT, respectively.

The energy storage properties W, W_{rec} and η are calculated from equations 2-4, given in Fig. 11. With increasing electric field, the values of W and W_{rec} increase for all studied compositions (Fig. 11a,b), the highest values of which are 4.1, 2.43, 1.16, 0.75 J/cm^3 and 1.82, 1.53, 0.87, 0.66 J/cm^3, respectively. At the same time, the values of η slightly decrease for BN15F-BT, BN30F-BT and BN40F-BT but increase for BN20F-BT (Fig. 11c). As Nd concentration increases, W and W_{rec} decrease significantly at an electric field of 170 kV/cm, with the values of η reaching a maximum of 87.8% for BN40F-BT (Fig. 11d).

A comparison of energy-storage properties among several lead-free FE and mutiferroic ceramics is given in Table II. BN15F-BT has the highest values of P_{max} ~ 39.8 μC/cm^2, W ~ 4.1 J/cm^3 and W_{rec} ~ 1.82 J/cm^3 among all displayed lead-free ferroelectric ceramics with an electric field < 250 kV/cm. BN20F-BT has high values of W ~ 2.43 J/cm^3 and W_{rec} ~ 1.53 J/cm^3 with a medium value of η ~ 63%, whilst the values of W and W_{rec} for BN30F-BT and BN40F-BT are low but with much higher values of η (> 75%). According to equations 2 and 3, the large values of W ~ 4.1 J/cm^3 and W_{rec} ~ 1.82 J/cm^3 for BN15F-BT may be attributed to the higher BDS (180 kV/cm), P_{max} (39.8 μC/cm^2) and ΔP (30.7 μC/cm^2), as discussed in Fig. 10. The BDS of bulk ceramics is related to microstructural features, such as grain size, density (porosity), grain boundary and secondary phase. Tunkasiri et al. confirmed the relationship between BDS and grain size (G) of ceramics (equ. 7):[54]

$$\text{BDS} \propto \frac{1}{\sqrt{G}}. \qquad (7)$$

Gerson et al. and Wu et al. reported that the BDS of dielectric ceramics would reduce greatly with an increase in porosity and defects.[55,56] In this work, significant reduction of grain size and porosity is achieved by doping with Nd (Figs. 5 and 6), leading to a large BDS of ~ 180 kV/cm for BN15F-BT and ~ 190 kV/cm for BN20F-BT, BN30F-BT and BN40F-BT, respectively; the highest values of BDS in all reported BF-based bulk ceramics to our knowledge.[36-38] Furthermore, BF-based solid solutions possess intrinsically large P_{max} which increases for relaxor ferroelectrics with increase in electric field.[30,32-35] Consequently, the improvement in W and W_{rec} for BNxF-BT is attributed to both the large BDS and high P_{max} induced by Nd doping.

Owing to its promising energy storage properties in bulk samples, BN15F-BT was co-fired with Pt internal electrodes at 1010-1040°C for 2hrs to form multilayers consisting of 9 active layers, as shown in the inset of Fig. 12(a). The total thickness of multilayers is ~ 0.78 mm, the thickness of each sintered layer is ~ 32 μm and the active area of each electrode is ~ 33 mm^2. The unipolar P-E loops under different electric fields at RT and the in-situ temperature dependence of unipolar P-E loops at an electric field of 300 kV/cm per layer are shown in Fig. 12(a, b), respectively. The corresponding values of P_{max}, P_r and ΔP as a function of electrical field and temperature are given in Fig. 13. The energy storage properties W, W_{rec} and η are also calculated and plotted in Fig. 12(c,d). With increase in electric field, the shape of P-E loops becomes slimmer, and the values of P_{max} and ΔP increased significantly with a slight increase in P_r (Fig. 13a), resulting in enhanced values of W, W_{rec} and η (Fig. 12c). The highest values of W ~ 8.75 J/cm^3, W_{rec} ~ 6.74 J/cm^3 and η ~ 77% for multilayers were obtained with an electric field of 540 kV/cm, which is one of the highest reported energy densities for ceramic capacitors.[57-60] As temperature increased, P-E loops became saturated at ~150 °C, leading to an increase of P_{max} and P_r (Fig. 13b), which was attributed to an easier field induced transition from a relaxor to a ferroelectric state.[32] The value of W consistently increased with temperature, while W_{rec} and η increased initially before decreasing after reaching maxima of 3.84 J/cm^3 and 76% at 100 °C, Fig. 12(d). The variation in W_{rec} is ~ 15% in a temperature range between RT and 125 °C, which is attractive for commercial applications.

The in-situ temperature dependence of leakage current density (J) of multilayers as a function of applied field is shown in Fig. 14. The value of J at RT is found to be on the order of 10^{-7} A/cm^2 in the high field region, which is at least one order smaller than that reported BF-based ceramics.[61,62] With the increase of temperature from RT to 150 °C, the value of J consistently increases, indicating increased conductivity at high temperatures.

The discharge behaviour of multilayers under different electric voltages is given in Fig. 15. The value of current is found to increase with the increase of voltage from 300 V to 900 V and all the discharge processes last about 10 μs, as shown in Fig. 15(a). The discharge time $\tau_{0.9}$ is defined as the time for the discharge energy in the load to achieve 90% of the final value from

the discharge profiles, which could be obtained from the curves of discharge energy density as a function of discharge time (Fig. 15b). The $\tau_{0.9}$ of multilayers under different voltages is less than 4 μs, indicating that 90% of the discharge energy density is released with this time period.

A comparison of W_{rec} and η among lead-based and lead-free ceramics/capacitors is summarized and plotted in Fig. 16. W_{rec} generally increases with electric field (Fig. 16a), while η decreases with larger values of W_{rec} (Fig. 16b). Lead-based ceramics still have higher values of W_{rec} compared to the lead-free ceramics (Fig. 16a) but the multilayers fabricated in this contribution possess the largest value of W_{rec} ~ 6.74 J/cm^3 with high η ~ 77% amongst lead-based and lead-free compositions at < 600 kV/cm (Fig. 16).

4. Conclusion

In this work, dense Nd doped BF-BT lead-free ceramics with $\rho_r \geq 95\%$ were prepared using a conventional solid state route. As Nd concentration increased, the BF-BT gradually transformed from a two phase mix of *R3c* and *PC* phases to a single *PC* phase, accompanied by a decrease of T_C/T_m and ferroelectric/piezoelectric/strain properties. The domain structure gradually altered in a manner consistent with the change in structure and phase assemblage from coarse herringbones-type domains, fine herringbones-type domains and complex domains to nano-sized domains and finally to nominally domain free state. This was accompanied by a reduction in the intensity of ½{*ooo*} superstructure reflections associated with octahedral tilting, despite a decrease in the average tolerance factor as Nd concentration increased. This unusual effect is attributed to frustration of long range tilting due to competing local distortions (phases) within the solid solution. The highest values of d_{33} ~ 140 pC/N, P_r ~ 35 μC/cm^2, E_C ~ 53.9 kV/cm, S_{max} ~ 0.14% and d_{33}* = 200 pm/V were obtained for the compositions with Nd concentration < 7.5%. Furthermore, the average grain size of BNF-BT was reduced from 6.3 μm for BF-BT to 1.9 μm for BN40F-BT, with an increase of ρ_r from 95% for BF-BT to 97.6% for BN40F-BT, leading to high BDS (180 kV/cm^3 for BN15F-BT and 190 kV/cm^3 for BN20F-BT, BN30F-BT, BN40F-BT) and large $P_{max}/\Delta P$ (39.8, 23.5, 11.6, 7.8 μC/cm^2 and 30.7, 20.4, 10.7, 7.6 μC/cm^2 for BN15F-BT, BN20F-BT, BN30F-BT and BN40F-BT, respectively). As electric field increased, *W* and

W_{rec} increased for all studied compositions, with η changing only slightly. As Nd concentration increased, W and W_{rec} decreased significantly, with η increasing greatly. The largest values of $W \sim 4.1$ J/cm^3 and $W_{rec} \sim 1.82$ J/cm^3 were achieved for BN15F-BT, while the maximum η of 87.8% was obtained for BN40F-BT. BN15F-BT multilayers consisting of 9 active layers were fabricated. The highest values of $W \sim 8.75$ J/cm^3, $W_{rec} \sim 6.74$ J/cm^3 and $\eta \sim 77\%$ were obtained at an electric field of 540 kV/cm, with a variation of ~ 15% for the value of W_{rec} from RT to 125 °C, values attractive for commercial applications.

Acknowledgements

We acknowledge the Engineering and Physical Sciences Research Council (EP/N010493/1 and EP/L017563/1) and National Natural Science Foundation of China (51402005) for funding and supporting this work.

References

1. C. Liu, F. Li, L. P. Ma and H. M. Cheng, Adv. Mater., 2010, **22**, E28–E62.
2. I. Hadjipaschalis, A. Poullikkas and V. Efthimiou, Renew. Sust. Energy Rev., 2009, **13**, 1513–1522.
3. H. Chen, T. N. Cong, W. Yang, C. Tan, Y. Li and Y. Ding, Prog. Nat. Sci., 2009, 19, 291–312.
4. G. R. Love, J. Am. Ceram. Soc., 1990, **73**, 323–328.
5. S. Kwon, W. Hackenberger, E. Alberta, E. Furman and M. Lanagan, IEEE Electr. Insul. Mag., 2011, **27**, 43–55.
6. W. B. Hu, Y. Liu, R. L. Withers, T. J. Frankcombe, L. Noren, A. Snashall, M. Kitchin, P. Smith, B. Gong, H. Chen, J. Schiemer, F. Brink and J. W. Leung, Nat. Mater., 2013, **12**, 821–826.
7. Q. Li, G. Zhang, F. Liu, K. Han, M. R. Gadinski, C. Xiong and Q. Wang, Energy Environ. Sci., 2015, **8**, 922–931.
8. B. Chu, X. Zhou, K. Ren, B. Neese, M. Lin, Q. Wang, F. Bauer and Q. M. Zhang, Science, 2006, 313, 334-336.
9. Q. Li, L. Chen, M. R. Gadinski, S. Zhang, G. Zhang, H. Li, A. Haque, L. Chen, T. Jackson and Q. Wang, Nature, 2015, 523, 576.

10. L. Zhang, S. Jiang, B. Fan and G. Zhang, J. Alloys Compd., 2015, 622, 162–165.
11. Z. Liu, X. Chen, W. Peng, C. Xu, X. Dong, F. Cao, and G. Wang, Appl. Phys. Lett., 106, 262901-4pp (2015)
12. Q. Zhang, H. Tong, J. Chen, Y. Lu, T. Yang, X. Yao, and Y. He, Appl. Phys. Lett., 109, 262901-4pp (2016)
13. R. Xu, B. Li, J. Tian, Z. Xu, Y. Feng, X. Wei, D. Huang, and L. Yang, Appl. Phys. Lett., 110, 142904 (2017)
14. Q. Zhang, J. Chen, Y. Lu, T. Yang, X. Yao, and Y. He, J. Am. Ceram. Soc., 99 [12] 3853–3856 (2016)
15. Q. L. Zhao, H. Lei, G. P. He, J. J. Di, D. W. Wang, P. P. Tan, H. B. Jin and M. S. Cao, Ceram. Int., 2016, **42**, 1314–1317.
16. J. Rodel, K. G. Webber, R. Dittmer, W. Jo, M. Kimura and D. Damjanovic, J. Eur. Ceram. Soc., 2015, **35**, 1659–1681.
17. J. G. Wu, D. Q. Xiao and J. G. Zhu, Chem. Rev., 2015, **115**, 2559–2595.
18. D. W. Wang, F. Hussain, A. Khesro, A. Feteira, Y. Tian, Q. L. Zhao and I. M. Reaney, J. Am. Ceram. Soc., 2017, **100**, 627–637.
19. W. B. Li, D. Zhou, L. X. Pang, R. Xu and H. H. Guo, J. Mater. Chem. A, 2017, **5**, 19607–19612.
20. B. B. Liu, X. H. Wang, Q. C. Zhao and L. T. Li, J. Am. Ceram. Soc., 2015, 98, 2641–2646.
21. Q. M. Zhang, L. Wang, J. Luo, Q. Tang, and J. Du, Int. J. Appl. Ceram. Technol., 2010, **7**, E124–E128.
22. Y. H. Huang, Y. J. Wu, W. J. Qiu, J. Li and X. M. Chen, J. Eur. Ceram. Soc., 2015, **35**, 1469–1476.
23. W. B. Li, D. Zhou and L. X. Pang, Appl. Phys. Lett., 2017, **110**, 132902-5pp.
24. T. Wang, L. Jin, C. C. Li, Q. Y. Hu and X. Y. Wei, J. Am. Ceram. Soc., 2015, **98**, 559–566.
25. Q. Y. Hu, L. Jin, T. Wang, C. C. Li, Z. Xing and X. Y. Wei, J. Alloys Compd., 2015, **640**, 416–420.
26. Z. B. Shen, X. H. Wang, B. C. Luo and L. T. Li, J. Mater. Chem. A, 2015, **3**,18146–18153.
27. L. W. Wu, X. H. Wang and L. T. Li, RSC Adv., 2016, **6**, 14273–14282.
28. Q. Xu, J. Xie, Z. C. He, L. Zhang, M. H. Cao, X. D. Huang, M. T. Lanagan, H. Hao, Z. H. Yao, H. X. Liu, J. Eur. Ceram. Soc., 2017, **37**, 99–106.

29. Q. Xu, H. X. Liu, L. Zhang, J. Xie, H. Hao, M. H. Cao, Z. H. Yao and M. T. Lanagan, RSC Adv., 2016, **6**, 59280–59291.
30. Z. T. Yang, H. L. Du, S. B. Qu, Y. D. Hou, H. Ma, J. F. Wang, J. Wang, X. Y. Wei and Z. Xu, J. Mater. Chem. A, 2016, **4**, 13778–13785.
31. T. Q. Shao, H. L. Du, H. Ma, S. B. Qu, J. Wang, J. F. Wang, X. Y. Wei and Z. Xu, J. Mater. Chem. A, 2017, **5**, 554–563.
32. D. W. Wang, A. Khesro, S. Murakami, A. Feteira, Q. L. Zhao and I. M. Reaney, J. Eur. Ceram. Soc., 2017, **37**, 1857–1860.
33. Q. J. Zheng, L. L. Luo, K. H. Lam, N. Jiang, Y. Q. Guo and D. M. Lin, J. Appl. Phys., 2014, **116**, 184101-11pp.
34. M. H. Lee, D. J. Kim, J. S. Park, S. W. Kim, T. K. Song, M. H. Kim, W. J. Kim, D. Do and I. K. Jeong, Adv. Mater., 2015, **27**, 6976–6982.
35. H. B. Yang, C. R. Zhou, X. Y. Liu, Q. Zhou, G. H. Chen, W. Z. Li and H. Wang, J. Eur. Ceram. Soc., 2013, **33**, 1177–1183.
36. T. Wang, L. Jin, Y. Tian, L. L. Shu, Q. Y. Hu and X. Y. Wei, Mater. Lett., 2014, **137**, 79–81.
37. D. G. Zheng, R. Z. Zuo, D. S. Zhang and Y. Li, J. Am. Ceram. Soc., 2015, **98**, 2692–2695.
38. D. G. Zheng and R. Z. Zuo, J. Eur. Ceram. Soc., 2017, **37**, 413–418.
39. B. Xu, J. Iniguez and L. Bellaiche, Nat. Commun., 2017, **8**, 15682-8pp.
40. A. Khesro, D. W. Wang, F. Hussain, D. C. Sinclair, A. Feteira, and I. M. Reaney, Temperature stable and fatigue resistant lead-free ceramics for actuators, Appl. Phys. Lett., 2016, 109, 142907-5pp.
41. D. W. Wang, M. L. Wang, F. B. Liu, Y. Cui, Q. L. Zhao, H. Sun, H. B. Jin and M. S. Cao, Ceram. Int., 2015, **41**, 8768–8772.
42. Y. Li, W. Q. Cao, J. Yuan, D. W. Wang and M. S. Cao, J. Mater. Chem. C, 2015, **3**, 9276–9282.
43. C. Larson and R. B. Von Dreele, Los Alamos: Los Alamos National Laboratory Report LAUR; 2004.
44. H. Toby, J. Appl. Cryst., 2001, **34**, 210–213.
45. B. Jaffe, W. R. Cook, and H. Jaffe, Piezoelectric Ceramics. Academic, London-New York, 1971.

46. C. W. Huang, L. Chen, J. Wang, Q. He, S. Y. Yang, Y. H. Chu, R. Ramesh, Phys. Rev. B, 2009, **80**, 140101-4pp.
47. D. I. Woodward, I. M. Reaney, Acta Cryst., 2005, **61**, 387-399.
48. R. D. Shannon, Acta Cryst., 1976, **A32**, 751-767.
49. S. Karimi, I. M. Reaney, I. Levin, I. Sterianou, Appl. Phys. Lett., 2009, **94**, 112903-3p.
50. D. C. Arnold, K. S. Knight, F. D. Morrison, P. Lightfoot, Phys. Rev. Lett., 2009, **102**, 027602-4pp.
51. P. M. Woodward, Acta Cryst., 1997, **853**: 44-66.
52. S. Karimi, I. M. Reaney, Y. Han, J. Pokorny, I. Sterianou, J. Mater. Sci., 2009, **19**, 5102-5112.
53. D. W. Wang, M. S. Cao and S. J. Zhang, J. Am. Ceram. Soc., 2012, **95**, 3220–3228.
54. T. Tunkasiri and G. Rujijanagul, J. Mater. Sci. Lett., 1996, **15**, 1767–1769.
55. R. Gerson and T.C. Marshall, J. Appl. Phys., 1959, **30**, 1650–1953.
56. Y. J. Wu, Y. H. Huang, N. Wang, J. Li, M. S. Fu and X. M. Chen, J. Eur. Ceram. Soc., 2017, **7**, 2099–2104.
57. H. Ogihara, C. A. Randall and S. Trolier-McKinstry, J. Am. Ceram. Soc., 2009, **92**, 1719–1724.
58. Y. Gao, H. X. Liu, Z. H. Yao, H. Hao, Z. Y. Yu and M. H. Cao, Ceram. Inter., 2017, **43**, 8418–8423.
59. D. P. Shay, N. J. Podraza, N. J. Donnelly and C. A. Randall, J. Am. Ceram. Soc., 2012, **95**, 1348–1355.
60. H. Lee, J. R. Kim, M. J. Lanagan, S. Trolier-McKinstry and C. A. Randall, J. Am. Ceram. Soc., 2013, **96**, 1209–1213.
61. Y. Guo, P. Xiao, R. Wen, Y. Wan, Q. Zheng, D. Shi, K. H. Lam,b M. Liu and D. Lin, J. Mater. Chem. C, 2015, **3**, 5811.
62. N. Liu, R. Liang, Z. Liu, Z. Zhou, C. Xu, G. Wang, X. Dong, Appl. Phys. Lett., 2017, **110**, 112902.
63. H. Tao, W. Wu and J. G. Wu, J. Alloys Compd., 2016, **689**, 759–766.

Table I. Refined structural parameters of BNxF-BT ceramics

Composition	Space	Lattice parameters (Å)			Volume (Å^3)	Phase	R factors (%)		
x	group	a	b	c		fraction (%)	R_{wp}	R_p	χ^2
0	R3c	5.6328	5.6328	13.8800	381.389	65.2^R	9.6	7.3	1.8
	Pm$\bar{3}$m	4.0015	4.0015	4.0015	64.073	34.8^C			
2.5	R3c	5.6241	5.6241	13.8798	380.209	37.8^R	9.9	7.5	3.7
	Pm$\bar{3}$m	3.9880	3.9880	3.9880	63.425	62.2^C			
5	R3c	5.6444	5.6444	13.7664	379.821	27.9^R	8.7	6.9	1.8
	Pm$\bar{3}$m	3.9812	3.9812	3.9812	63.100	72.1^C			
7.5	Pm$\bar{3}$m	3.9816	3.9816	3.9816	63.121		10.3	8.2	2.0
10	Pm$\bar{3}$m	3.9793	3.9793	3.9793	63.012		8.6	6.6	1.8
15	Pm$\bar{3}$m	3.9736	3.9736	3.9736	62.739		8.8	6.9	1.7
20	Pm$\bar{3}$m	3.9698	3.9698	3.9698	62.563		9.9	7.4	1.5
30	Pm$\bar{3}$m	3.9602	3.9602	3.9602	62.107		10	7.5	1.6
40	Pm$\bar{3}$m	3.9531	3.9531	3.9531	61.777		10.9	7.9	1.8

Table II. Comparison of polarization and energy storage properties among lead-free and multiferroic ceramics.

Compounds	E (kV/cm)	P_{max} ($\mu C/cm^2$)	ΔP_r ($\mu C/cm^2$)	W (J/cm^3)	W_{rec} (J/cm^3)	η (%)	Ref
BF-BT-Nb	90	25	19.7	/	0.71	/	36
BF-BT-BMN	125	38	32.3	2.08	1.56	75	37
BF-BT-LMT	130	37.5	33.3	2.02	1.66	82	38
BT-BMN	210	21	16.3	1.92	1.7	88.5	23
BT-BY	93	~17	~16	0.86	0.71	82.6	26
BST	230	~12	~11	1.3	1.13	86.8	56
BNT-BT-KN	168	~40	~30	/	1.72	/	28
BNT-BT-NT	100	~33	~29	1.6	1.2	74.8	29
KNNS-BNH	129	23.47	18.61	/	0.54	/	63
KNN-BMN	300	~41.7	~33.7	6.5	4.08	62.8	30
KNN-ST	400	33.3	~16	7.76	4.03	52	31
BN15F-BT	170	39.8	30.7	4.1	1.82	41.3	this work
BN20F-BT	180	23.5	20.4	2.43	1.53	63	this work
BN30F-BT	180	11.6	10.7	1.16	0.87	75.3	this work
BN40F-BT	180	7.8	7.6	0.75	0.66	87.8	this work

Fig. 1. Room temperature XRD patterns of BNxF-BT in the 2θ range of 20°~70°.

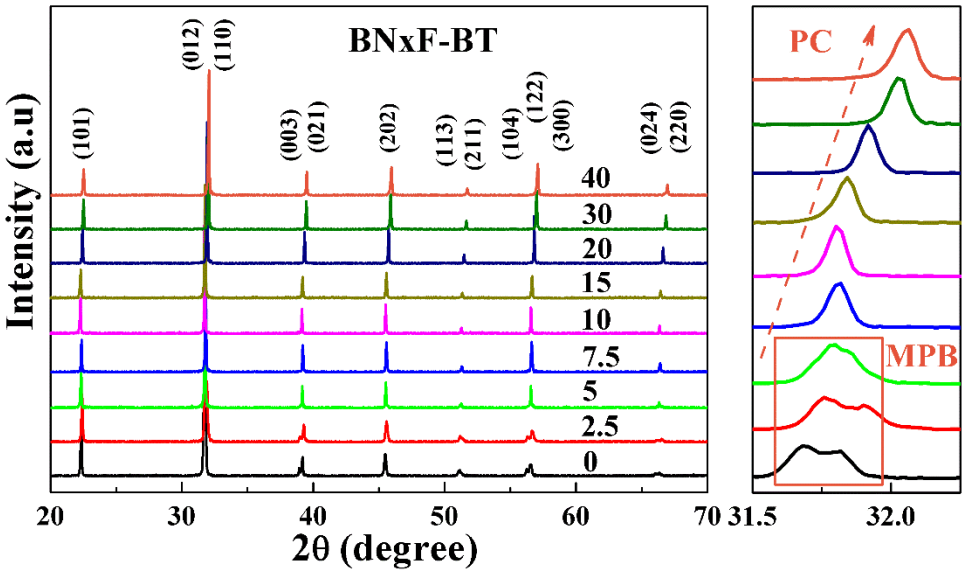

Fig. 2. Rietveld refinement analysis of (a) BF-BT and (c) BN10F-BT using the GSAS+EXPGUI package; (c) unit cell volume and (d) lattice parameters of BNxF-BT as a function of Nd concentration. Note. Error bars are smaller than the symbols.

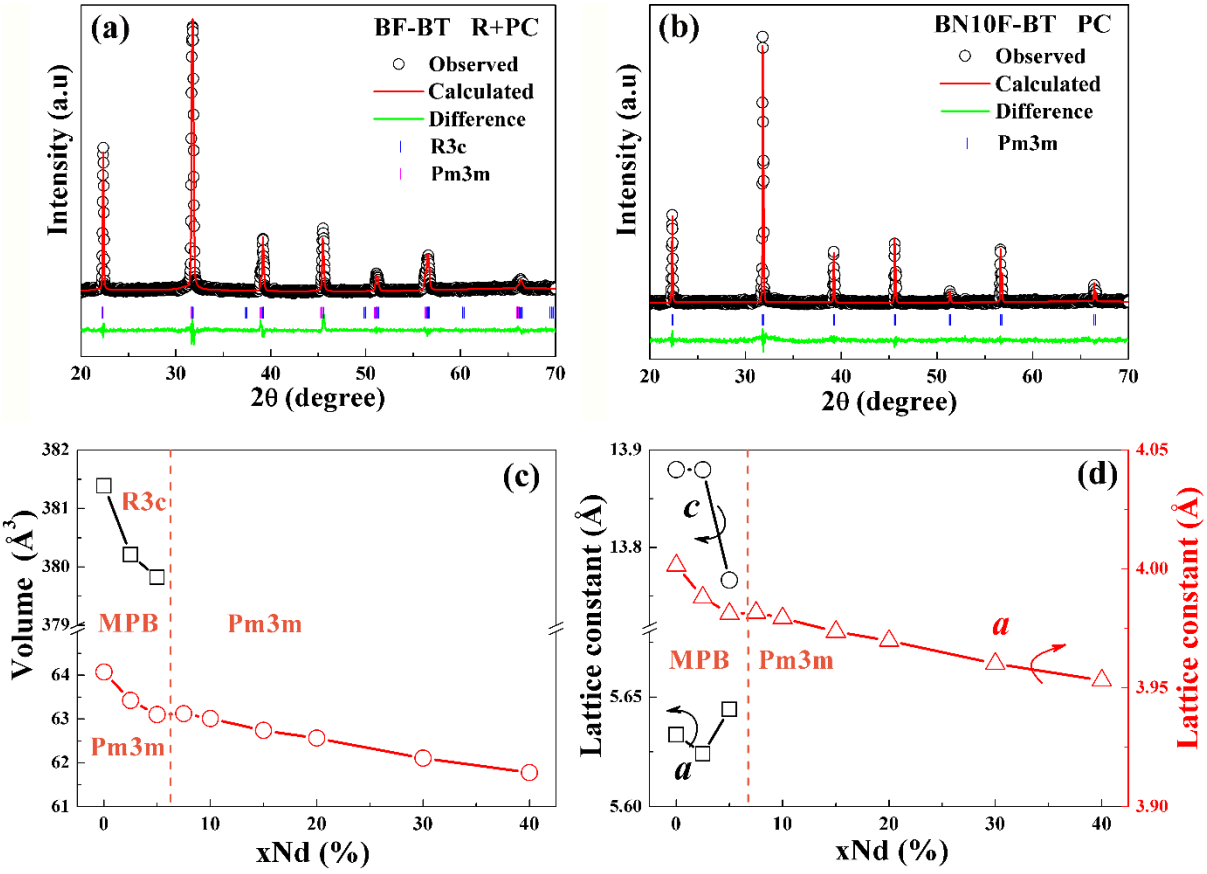

Fig. 3. Transmission electron microscopy images of the domain structure in BF-BT, BN5F-BT and BN10F-BT.

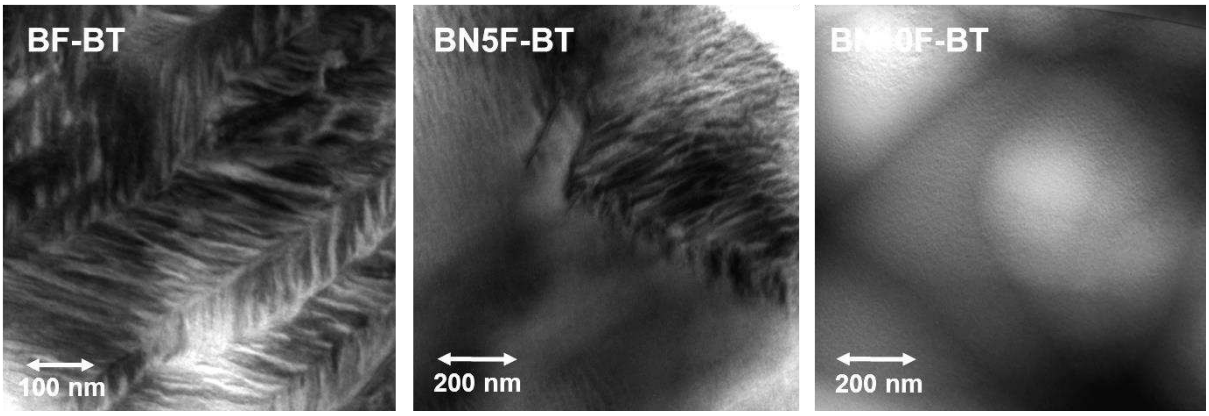

Fig. 4. <110> zone axis diffraction patterns illustrating the decrease in intensity of ½{ooo} antiphase tilt reflection as a function of increasing Nd concentration.

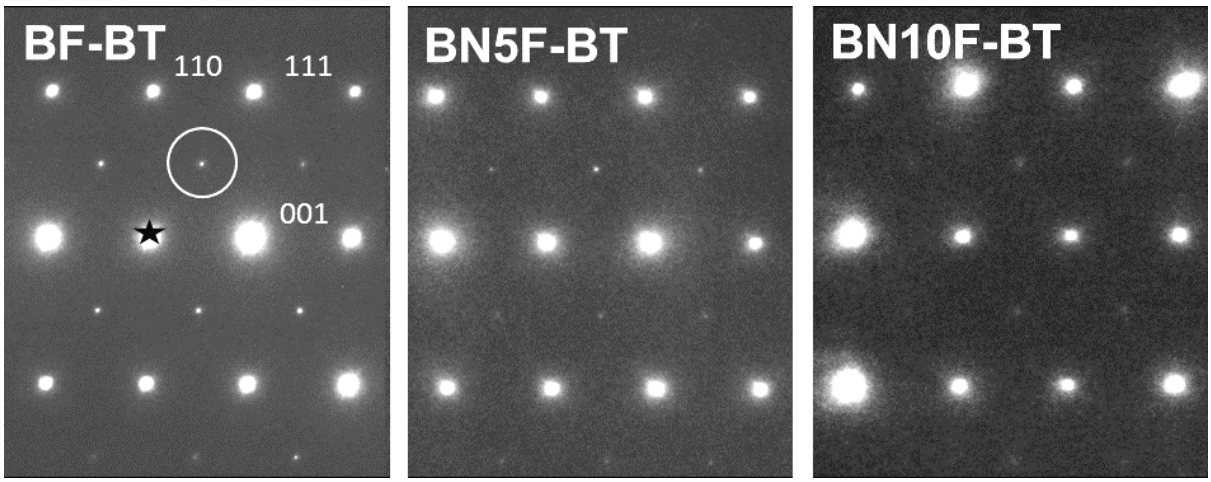

Fig. 5. Scanning electron microscopy images of BNxF-BT: (a) BF-BT, (b) BN2.5F-BT, (c) BN5F-BT, (d) BN7.5F-BT, (e) BN10-BT, (f) BN15F-BT, (g) BN20F-BT, (h) BN30F-BT and (i) BN40F-BT; The grain size distributions of BNxF-BT are in the inset in each image.

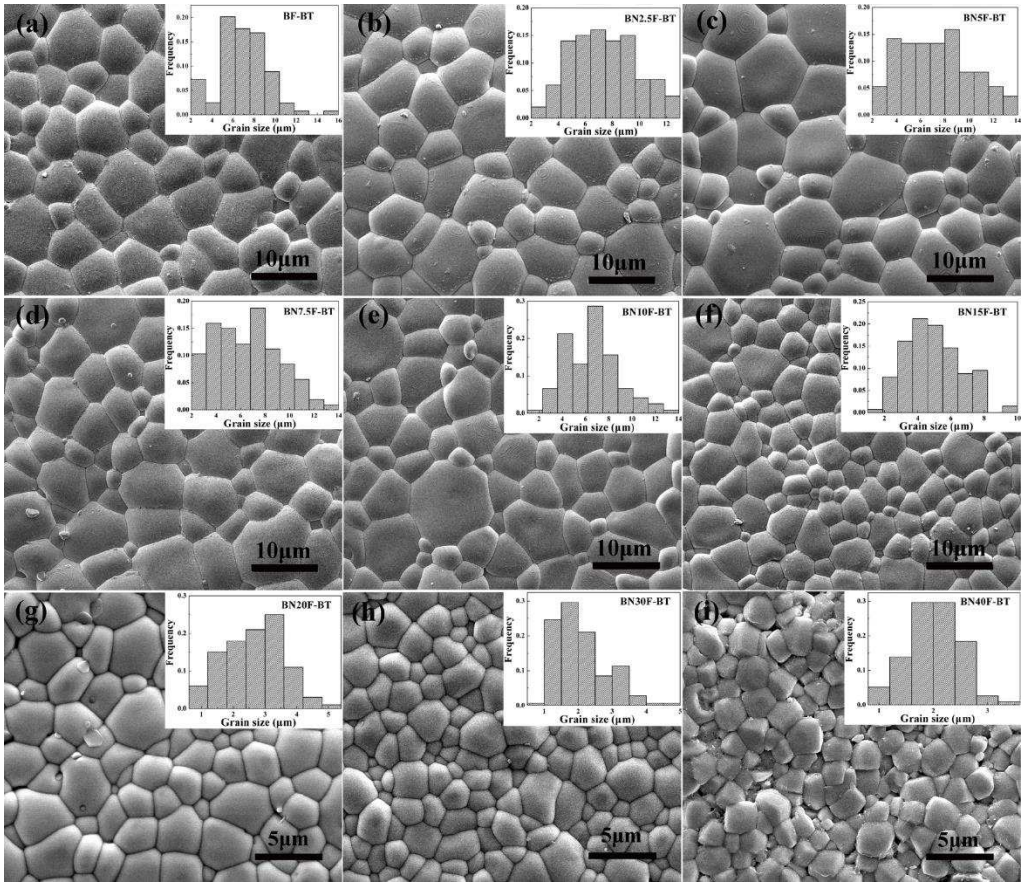

Fig. 6. Average grain size and relative density of BNxF-BT as a function of Nd concentration.

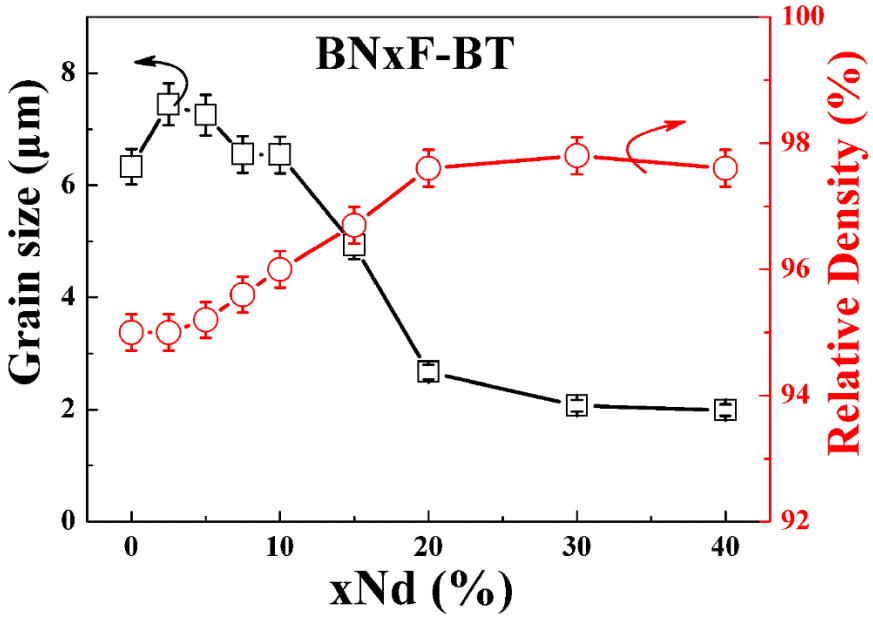

Fig. 7. Temperature dependence of (a) ε_r and (b) tanδ for BNxF-BT; T_C/T_m as a function of Nd concentration is in the inset of (b). Note. Error bars are smaller than the symbols.

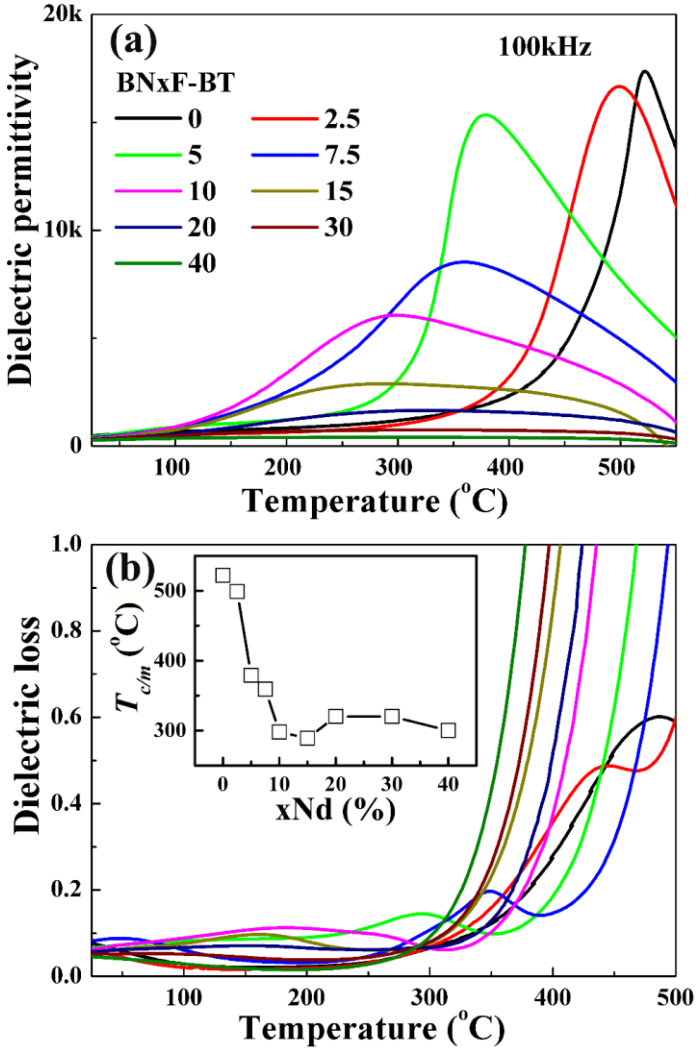

Fig. 8. High electric field (a) bipolar polarization hysteresis loops and (b) unipolar strain loops for BNxF-BT; (c) corresponding P_r and E_C as a function of Nd concentration; (d) corresponding d_{33}^* and SH as a function of Nd concentration; d_{33} as a function of Nd concentration is in the inset of (c).

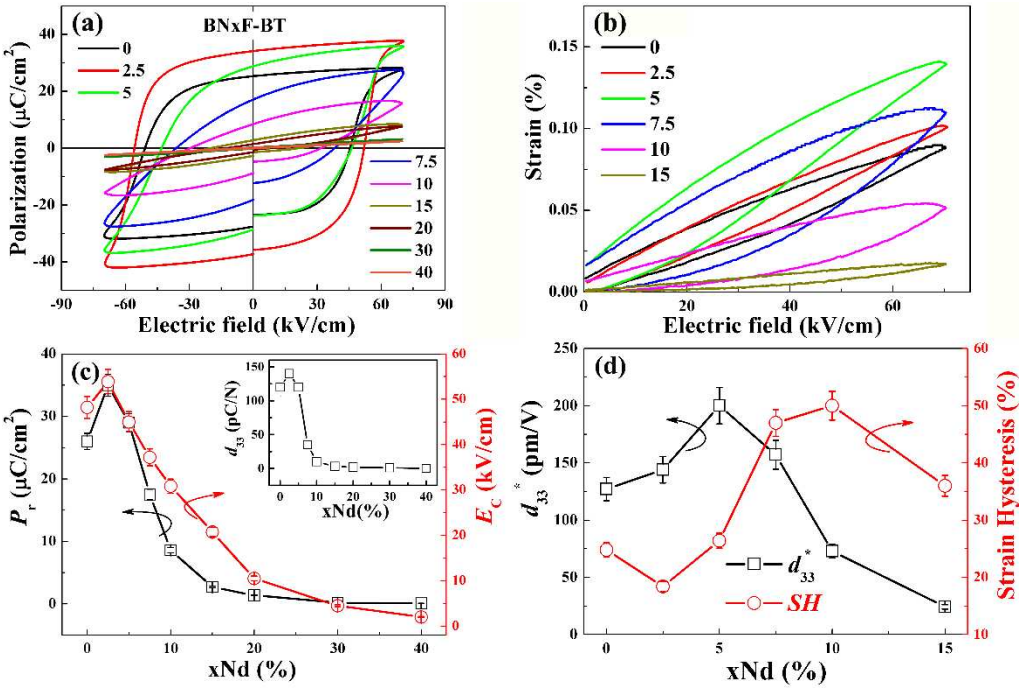

Fig. 9. Unipolar P-E loops under different electric fields for (a) BN15F-BT, (b) BN20F-BT, (c) BN30F-BT and (d) BN40F-BT.

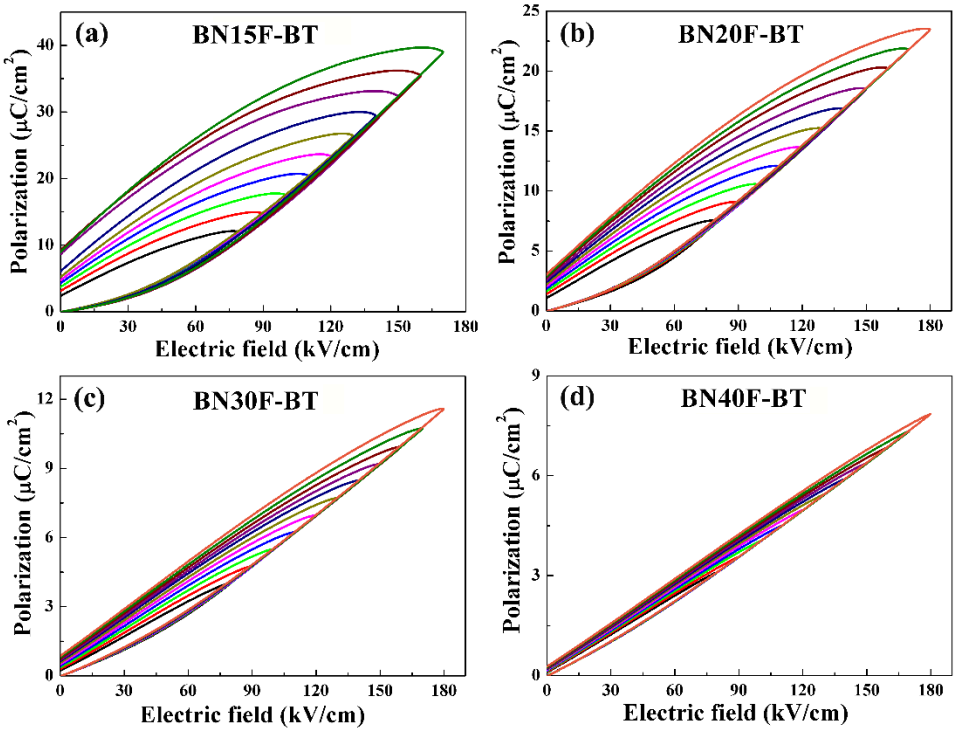

Fig. 10. P_{max}, P_r and ΔP as a function of electrical field for (a) BN15F-BT, (b) BN20F-BT, (c) BN30F-BT and (d) BN40F-BT; P_{max}, P_r and ΔP as a function of Nd concentration at 170 kV/cm is in the inset of (d).

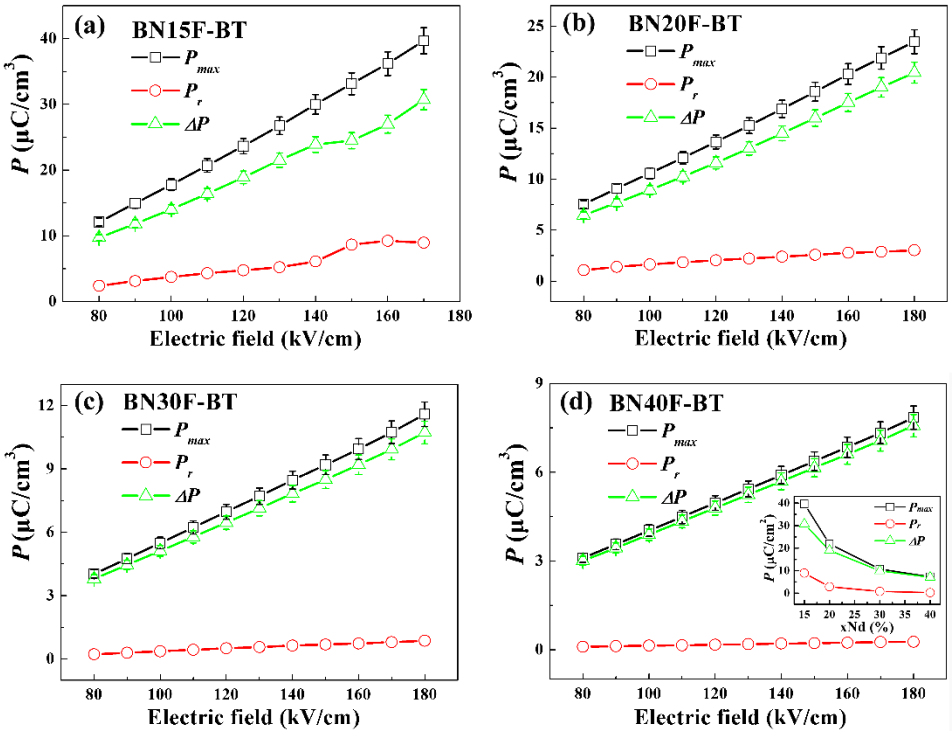

Fig. 11. (a) W, (b) W_{rec} and (c) η of BN15F-BT, BN20F-BT, BN30F-BT and BN40F-BT as a function of electrical field; (e) W, W_{rec} and η as a function of Nd concentration at 170 kV/cm.

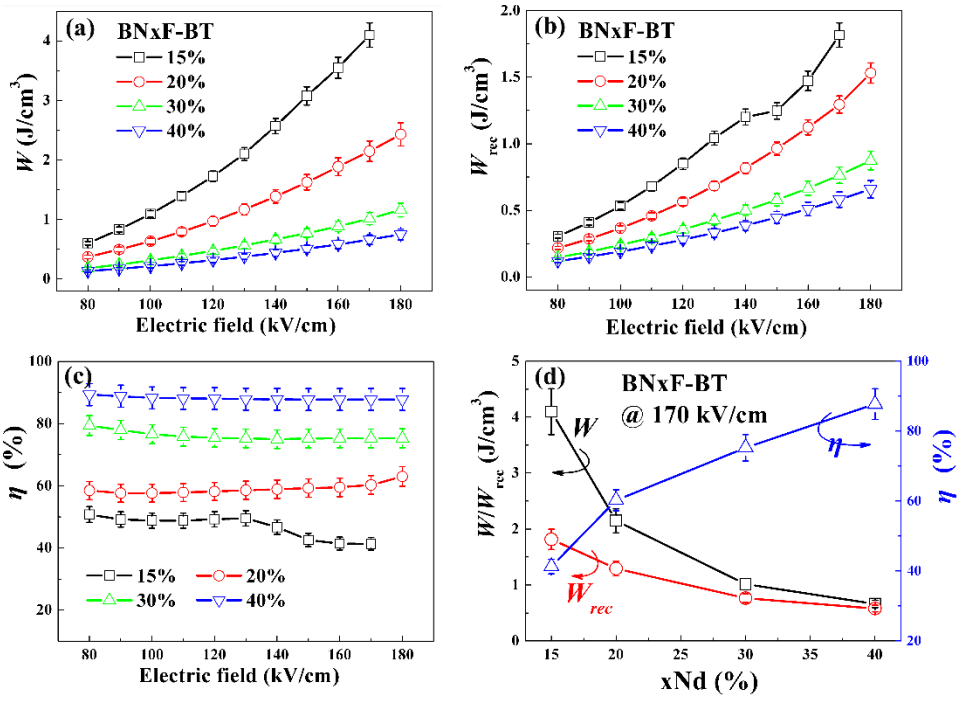

Fig. 12. (a) Unipolar P-E loops of multilayers under different electric fields at RT, (b) in-situ temperature dependence of unipolar P-E loops of multilayers at an electric field of 300 kV/cm, (c) W, W_{rec} and η of multilayers as a function of electric field at RT, and (d) W, W_{rec} and η of multilayers as a function of temperature at 300 kV/cm; SEM image of multilayers is in the inset of (a).

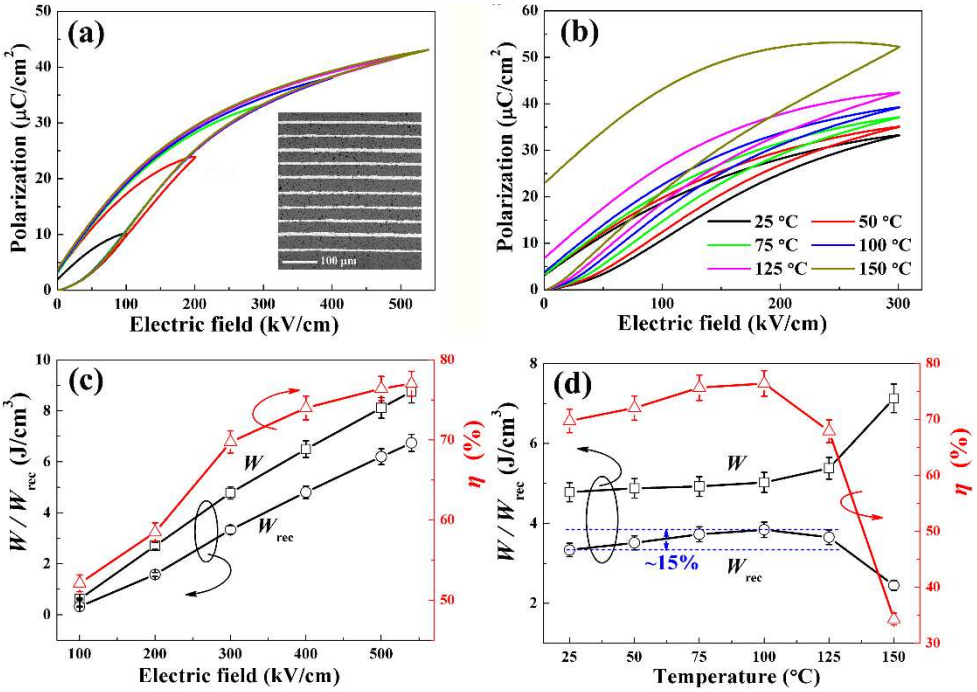

Fig. 13. P_{max}, P_r and ΔP of multilayers (a) as a function of electrical field at RT and (b) as a function of temperature at 300 kV/cm.

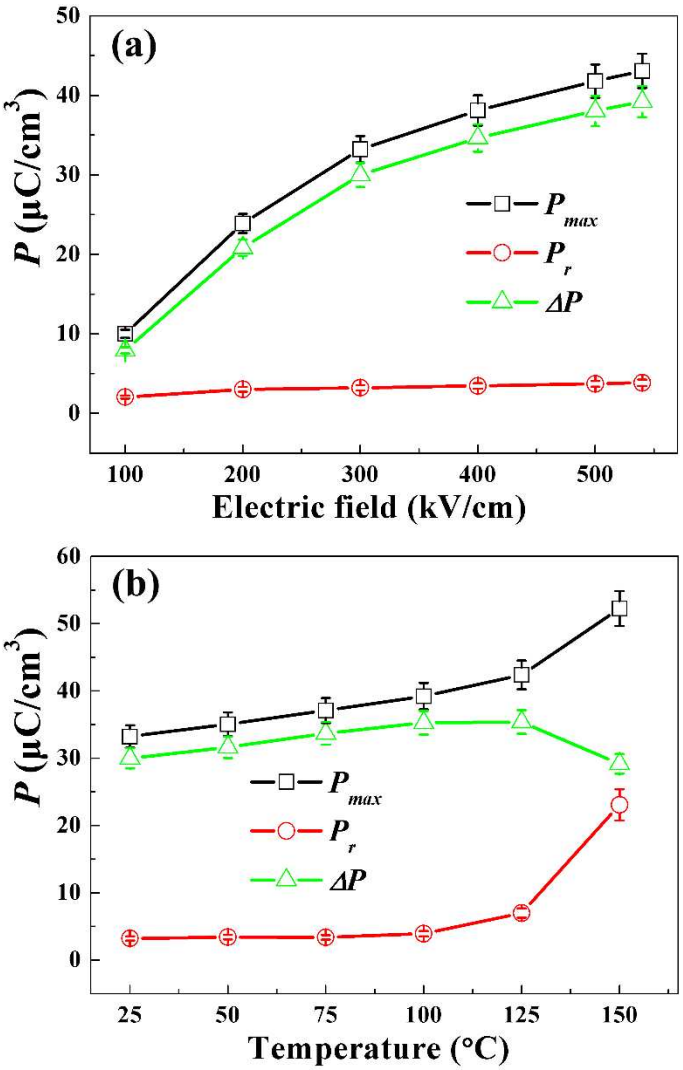

Fig. 14. The in-situ temperature dependence of leakage current density (J) of multilayers as a function of applied field.

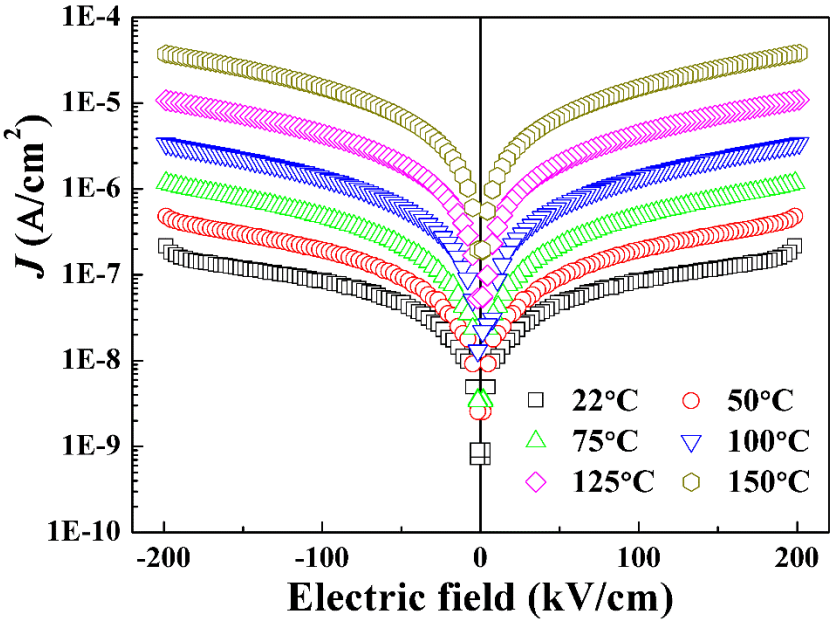

Fig. 15. The discharging behaviour of multilayers under different electric voltages (a) time dependence of the pulsed discharge current and (b) time dependence of the discharge energy density.

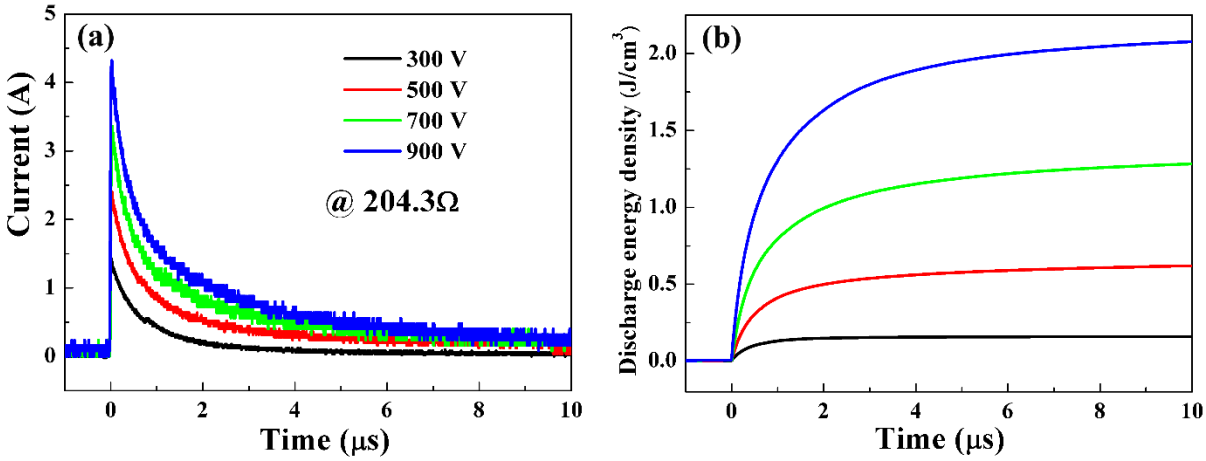

Fig. 16. Comparison of energy-storage properties among lead-based and lead-free ceramics/capacitors.

10-15, 19-31, 36-38, 56-60, 63